Green-Emitting Powders of Zero-Dimensional Cs_4PbBr_6: Delineating the Intricacies of the Synthesis and the Origin of Photoluminescence

Aniruddha Ray[†,‡], **Daniela Maggioni**[∥], **Dmitry Baranov**[†], **Zhiya Dang**[†], **Mirko Prato** , **Quinten A. Akkerman**[†], **Luca Goldoni**[⊥], **Enrico Caneva**[§], **Liberato Manna**[*,†], **Ahmed L. Abdelhady**[*,†]

[†]Nanochemistry Department, Istituto Italiano di Tecnologia, Via Morego 30, 16163 Genova, Italy

 Materials Characterization Facility, Istituto Italiano di Tecnologia, Via Morego 30, 16163 Genova, Italy

[⊥]Analytical Chemistry Lab, Istituto Italiano di Tecnologia, Via Morego 30, 16163 Genova, Italy

[‡]Dipartimento di Chimica e Chimica Industriale, Universitá degli Studi di Genova, Via Dodecaneso 31, 16146 Genova, Italy

[∥]Dipartimento di Chimica, Universitá degli Studi di Milano, Via Golgi 19, 20133 Milano, Italy

[§]UNITECH COSPECT (Comprehensive Substance Characterization via Advanced Spectrometry), Universitá degli Studi di Milano, Via Golgi 19, 20133 Milano, Italy

Abstract

A detailed investigation into the synthesis of green-emitting powders of Cs_4PbBr_6 and $CsPbBr_3$ materials by antisolvent precipitation from $CsBr$-$PbBr_2$ precursor solutions in dimethylformamide (DMF) and dimethyl sulfoxide (DMSO) is reported. Various solvated lead bromide and polybromide species ($PbBr_2$, $[PbBr_3]^-$, $[PbBr_4]^{2-}$, and possibly $[PbBr_5]^{3-}$ or $[PbBr_6]^{4-}$) are detected in the precursor solutions by optical absorbance and emission spectroscopies. The solvodynamic size of the species in solution is strongly solvent-dependent: ~1 nm species were detected in DMSO, while significantly larger species were observed in DMF by dynamic light scattering. The solvodynamic size of the lead bromide species plays a critical role in determining the Cs-Pb-Br composition of the precipitated powders: smaller species favor the precipitation of Cs_4PbBr_6, while larger species template the formation of $CsPbBr_3$ under identical experimental conditions. The powders have been characterized by [133]Cs and [207]Pb solid-state nuclear magnetic resonance, and [133]Cs sensitivity toward the different Cs environments within Cs_4PbBr_6 is demonstrated. Finally, the possible origins of green emission in Cs_4PbBr_6 samples are discussed. It is proposed that a two-dimensional Cs_2PbBr_4 inclusion may be responsible for green emission at

[*]Corresponding Authors: liberato.manna@iit.it (L.M.), ahmed.abdelhady@iit.it (A.L.A.).

Author Contributions
The manuscript was written through contributions of all authors. All authors have given approval to the final version of the manuscript.
Notes
The authors declare no competing financial interest.

~520 nm in addition to the widely acknowledged $CsPbBr_3$ impurity, although we found no conclusive experimental evidence supporting such claims.

All-inorganic lead halide semiconductors have recently attracted renewed research interest due to the various stoichiometries that can be crystallized from the same precursors. Lead halide compounds demonstrate structural tunability based on the connectivity of the $[PbX_6]^{4-}$ ($X = Cl^-$, Br^-, or I^-) octahedra that can form three-dimensional (3D) corner-sharing structures (perovskites), layered 2D networks, chains of 1D, and 0D isolated octahedral clusters.[1–5] In case of the organic-inorganic lead halide compounds, the size of the organic cation has been found to be one of the main factors determining the dimensionality of the octahedral framework. However, in the all-inorganic Cs-Pb-Br compounds, all three dimensionalities can be formed with the same Cs cation. Mixing CsBr and $PbBr_2$ in specific ratios and in appropriate solvents leads to the formation of pure or mixed structures of $CsPbBr_3$ (3D), $CsPb_2Br_5$ (2D), and Cs_4PbBr_6 (0D).[6] $PbBr_2$-rich conditions lead to the 2D tetragonal $CsPb_2Br_5$ phase, characterized by a sandwich structure with Cs^+ ions in between layers of $[Pb_2Br_5]^-$. On the other hand, under CsBr-rich conditions, a trigonal 0D Cs_4PbBr_6 structure is formed, which consists of disconnected $[PbBr_6]^{4-}$ octahedra separated by Cs^+ ions. An equimolar amount or a slight excess of $PbBr_2$ with respect to CsBr results in the formation of 3D $CsPbBr_3$ with an orthorhombic structure of corner-sharing $[PbBr_6]^{4-}$ octahedra, as in the organic-inorganic perovskites ($MAPbX_3$ and $FAPbX_3$; MA = methylammonium and FA = formamidinium) commonly used in optoelectronic applications. [7]

Cs_4PbBr_6-based materials have recently gained increased interest due to the reports of strong and stable green photoluminescence (PL) in their powder, thin-film, single crystal, and nanocrystal forms.[8–15] However, it was reported that Cs_4PbX_6 compounds are colorless[16] with band gaps in the UV region.[12] Specifically, Cs_4PbBr_6 has a matching experimental and theoretical band gap around 3.95 eV.[17–19] Hence, the origin of the green PL has been proposed to be either due to intrinsic defects within the wide band gap of Cs_4PbBr_6 [13–15] or due to the presence of 3D $CsPbBr_3$ nanocrystals.[19–24] Ling et al.[25] suggested that the 3D $CsPbBr_3$ phase is not the direct cause of the intense PL; instead, they proposed trap states at the interface between the two phases (3D and 0D) to be responsible for that intense green emission.

Herein, we explore reaction parameters governing the formation of Cs_4PbBr_6 and $CsPbBr_3$ phases from CsBr–$PbBr_2$ solutions and the origin of the green PL in the Cs_4PbBr_6 samples. The nature and solvodynamic size of the lead bromide species formed in solution varies with the coordination strength of the solvent and subsequently determines the composition of the formed Cs-Pb-Br powders: species with an ~1 nm solvodynamic radius (presumably isolated octahedra) were detected in dimethyl sulfoxide (DMSO) solutions of CsBr-$PbBr_2$ leading to the formation of the Cs_4PbBr_6 phase upon addition of an antisolvent, while larger species were detected in dimethylformamide (DMF) and resulted in the formation of the $CsPbBr_3$ phase. In addition to the solvent, the solvent-antisolvent pair and the absolute concentrations of the precursors are key parameters defining the structure of the precipitated material. For example, antisolvents such as tetrahydrofuran (THF) and dichloromethane (DCM)

precipitate mainly Cs_4PbBr_6 and $CsPbBr_3$ phases, respectively, from the $CsBr-PbBr_2$ solutions in DMSO when used in 1:6 (solvent:antisolvent by volume) ratios. Increasing the concentration of $CsBr-PbBr_2$ while keeping their molar ratio fixed (1:1) from 0.05 to 0.5 M in DMSO favors the formation of $CsPbBr_3$ at higher concentrations. In addition to the powder X-ray diffraction (XRD) technique commonly used for a structural and compositional identification of the materials, we apply [133]Cs and [207]Pb solid-state nuclear magnetic resonance (ssNMR) to the analysis of various Cs-Pb-Br precipitates. We found that [133]Cs ssNMR is more sensitive toward detecting relatively low impurity content of the different phases compared to its [207]Pb counterpart. The [133]Cs ssNMR results are in agreement with XRD data in terms of observed phases, but [133]Cs ssNMR could also distinguish between the two different Cs crystallographic positions in the 0D crystal. Finally, based on the observed absorbance in the visible region and the recurring green PL of Cs_4PbBr_6 samples, we hypothesize that 2D Cs_2PbBr_4 inclusion (not observed experimentally) may be responsible for green PL in addition to the widely acknowledged 3D impurity.

Experimental Section

Materials

CsBr (99.9%, Sigma-Aldrich), $PbBr_2$ (98%, Sigma-Aldrich), DMSO (99.9%, Sigma-Aldrich), DMF (99.8%, Sigma-Aldrich), THF (99.9%, Sigma-Aldrich), and DCM (99.8%, amylene stabilizer, Sigma-Aldrich).

Preparation of Cs-Pb-Br Powders

Generally, CsBr and $PbBr_2$ were dissolved in DMSO or DMF at the required ratio and at the required concentration by sonication for 1 h. Then, the solutions were filtered using a PTFE filter with 0.2 mm pore size, and the precipitation was carried out by quick injection of THF or DCM to the filtrate.

Characterization

The optical absorbance of the precursor solutions was recorded on a Varian Cary Eclipse UV–vis spectrophotometer. PLE and PL of precursor solutions were performed on a Varian Cary Eclipse fluorescence spectrophotometer. DLS was performed using a Zeta Sizer (Malvern Instruments) equipped with a 4.0 mW He–Ne laser operating at 633 nm and an avalanche photodiode detector in order to determine the average size of the precursors in the mother solution.

X-ray diffraction analysis was performed using a P Analytical Empyrean X-ray diffractometer equipped with a 1.8 kW Cu Ka ceramic X-ray tube and a PIXcel3D 2×2 area detector, operating at 45 kV and 40 mA. Cs-Pb-Br powders were studied under ambient conditions using a parallel beam in Bragg-Brentano geometry. XRD data was analyzed using HighScore 4.1 software from PANanalytical. Step sizes of 0.026° and 0.013° and scan speeds of 0.102 and 0.013°/s were used for the standard and slow scans, respectively.

PL and PLQY measurements on dried powders were conducted on an Edinburgh Instruments FLS920 fluorescence spectrometer equipped with a calibrated integrating sphere exciting at 405 nm. Absorbance measurements for the powder samples were carried out in a Cary 5000 spectrometer using the diffuse reflectance accessory. Optical microscopy of the 4:1 DMSO powder was performed on a Nikon 80i microscope equipped with a grayscale digital camera, a high-pressure mercury lamp (Nikon), and optical filters. The sample was prepared by mixing a small amount of the finely ground powder with a drop (~5 μL) of octadecene-1. The mixture was prepared on top of a rectangular microscope slide and covered with a thin glass coverslip. Confocal PL microscopy on the same sample was performed using a Nikon A1 confocal laser microscope with 488 nm excitation (Oxxius LBX-488 diode laser). The laser power setting was kept at 0.5%, and the resolution of a 32-channel spectral detector was set at 2.5 nm during the experiments. The spectrally resolved imaging data and the z-series used for a volume view reconstruction (Figure S8) were acquired (as *.ND2 files) using Nikon NIS-Elements High Content Software Analysis ver. 4.30.02 and viewed and processed in either Nikon NIS-Elements Viewer ver. 4.20.00 or ImageJ 1.51j8 as previously described.[26]

XPS measurements were carried out on a Kratos Axis UltraDLD spectrometer using a monochromatic Al Kα source (15 kV, 20 mA). The spectra were taken on a $300 \times 700\ \mu m^2$ area. Wide scans were collected with a constant pass energy of 160 eV and an energy step of 1 eV. High-resolution spectra were acquired at a constant pass energy of 10 eV and energy step of 0.1 eV. The binding energy scale was referenced to the C 1s peak at 284.8 eV. The spectra were analyzed using CasaXPS software (version 2.3.17). Samples were prepared by covering an indium substrate with the Cs-Pb-Br powder.

High-resolution transmission electron microscopy (HRTEM) analysis was carried out on a 200 kV TEM (JEOL JEM-2200FS) and a Bruker Quantax 400 system with an XFlash 5060 detector equipped on the same microscope was used for EDS analysis. The sample was prepared by dispersing the powders in THF before depositing on an ultrathin carbon film supported on holey carbon film-coated 400-mesh TEM copper grids.

Solid-state NMR (ssNMR) measurements were collected on a 500 MHz Bruker BioSpin NMR Spectrometer Avance 500, operating at a static field of 11.7 T and equipped with a 4 mm CPMAS probe by spinning the sample at the magic angle (MAS) with speed rates from 10 to 14 kHz. All samples were packed into zirconia (ZrO_2) rotors and closed with Kel-F caps (80 μL of internal volume). The working frequency of the ^{133}Cs nucleus was 65.598 MHz, and spectra were acquired by using a single-pulse sequence (zg) with a spectral width of 104166 Hz, wide enough to ensure a homogeneous irradiation of the whole spectrum. The optimal spinning speed (MAS) was achieved at 10 KHz; however, comparative spectra were also acquired at different spinning rates (12 and 14 KHz) to assign all sidebands in the spectrum and to exclude any possible signal impurity overlapping the manifold SSB. The NMR parameters used for ^{133}Cs experiments were 90° pulse length (p1) = 2.5 μs, repetition time (d1) = 3-60 s, and number of scans (ns) = 200-800. The working frequency of the ^{207}Pb nucleus was 104.63 MHz, and spectra were acquired by using a singlepulse sequence (solid echo with an echo time of 7 μs) with a spectral width of 1600 ppm (corresponding to 167.000 Hz), wide enough to allow a homogeneous irradiation of the whole spectrum but

not enough to cover the wide anisotropic chemical shift range, typical of such a nucleus. Different experiments were needed (with the same spectral width but changing the offset) to cover the whole possible range of detectable signals. The spinning speed (MAS) was optimized at 10 kHz, a value that returned resolved spectra. The NMR parameters used for ^{207}Pb experiments were the following: 90° pulse length (p1) = 2 μs, repetition time (d1) = 0.5 s, and ns = 28.000105.000. ^{133}Cs and ^{207}Pb shifts were referenced to solid CsBr (δ_{iso}=268.0 ppm vs CsCl: δ_{iso} = 223.2 ppm) and Pb(NO3)$_2$ (δ = -3490 ppm), respectively, which were used as external calibration standards.

Results and Discussion

CsBr-PbBr$_2$ Solutions in DMSO and DMF

PbBr$_2$-containing solutions in DMF and DMSO are precursors for the Cs$_4$PbBr$_6$ and CsPbBr$_3$ samples; thus, it is anticipated that the nature of the solvated species has an effect on the resulting material obtained from them. Steady-state optical spectroscopy is a simple method for investigation of the lead bromide speciation. Absorbance, photoluminescence (PL), and photoluminescence excitation (PLE) spectra of 0.05 M solutions of CsBr:PbBr$_2$ mixtures (1:1 molar ratio) in DMSO and DMF were collected and are reported in Figure 1. The DMSO solution showed an absorbance peak at 285 nm that is attributed to PbBr$_2$, while the DMF solution had a clear absorbance peak at 310 nm corresponding to [PbBr$_3$]$^-$ (Figure 1a), consistent with previous studies.[27,28] Both solutions showed an absorbance tail in the longer wavelength region (340–360 nm, inset in (Figure 1a), suggesting the possible formation of [PbBr$_4$]$^{2-}$ species.[27] Both [PbBr$_3$]$^-$ and [PbBr$_4$]$^{2-}$ species are emissive (at ~600 and 560 nm, respectively),[27,28] and their presence can be confirmed through selective wavelength excitation (Figure 1b). The DMSO solution emitted at 560 nm regardless of the excitation wavelength, indicating the presence of mainly [PbBr$_4$]$^{2-}$. On the other hand, the DMF solution exhibited emissions at 560 and 600 nm, confirming the presence of detectable amounts of both [PbBr$_3$]$^-$ and [PbBr$_4$]$^{2-}$ species. A relatively higher PL intensity of the DMF solution compared to DMSO under 360 nm excitation (Figure 1b) suggests a relatively higher concentration of [PbBr$_4$]$^{2-}$ species in DMF with respect to DMSO (consistent with a higher absorbance at around 360 nm). The presence of an extra PLE peak at 374 nm in the DMF solution (Figure 1b) that is redshifted relative to that of [PbBr$_4$]$^{2-}$ in the DMSO solution suggests that higher-order lead polybromide complexes, such as [PbBr$_5$]$^{3-}$ or [PbBr$_6$]$^{4-}$, might be present in DMF (by analogy with their iodide counterparts).[29]

We performed DLS measurements on both solutions to further investigate the discussed differences in lead bromide speciation between the two solvents. It was found that the DMSO solution contained roughly 1 nm-sized lead bromide species, while the DMF solution was composed of significantly larger clusters (Figure 1c). The large-sized clusters in the DMF solution could be due to an aggregation or polymerization of the lead bromide species because of the different solventsolute interaction between PbBr$_2$ and DMF compared to DMSO (similar to PbI$_2$ [29–31]). Our findings indicate that a change of solvent significantly alters the speciation and the solvodynamic size of the lead bromide species, as schematically summarized in Figure 1d. The results hold in the absence of CsBr, as summarized in the Supporting Information (see Figure S1 and accompanying discussion). Previously, the

changes in the solvodynamic size of the lead polyhalide species have been attributed to the relative ratio of salts (e.g., MAI:PbI$_2$; MA = methylammonium)[32] or to the effect of additives such as hydrohalic acids.[33] This is of high significance to the perovskite photovoltaic community as the solvodynamic size of the species present in the precursor solution influences the composition of the resulting material (see below) and subsequent optoelectronic properties of the devices.[32,33]

Cs$_4$PbBr$_6$ and CsPbBr$_3$ Formation

Next, we investigated the differences in the composition of the powders precipitated from the abovementioned CsBr-PbBr$_2$ solutions in DMSO and DMF. Using the equimolar (0.05 M each precursor) solutions in DMSO and DMF, the precipitation of the powders was done by a quick injection of 6 mL of tetrahydrofuran (THF) to 1 mL of the solution. Powders were then dried overnight in a vacuum oven at 40 °C. X-ray diffraction (XRD) patterns of the dried powders are plotted in Figure 2a along with the simulated patterns of Cs$_4$PbBr$_6$ and CsPbBr$_3$. It is observed that mainly the 0D trigonal phase was obtained from the DMSO solution with only low-intensity peaks corresponding to a 3D impurity, while 3D CsPbBr$_3$ was the main precipitate from the DMF solution with an extremely low contamination from the 0D phase (inset in Figure 2a). The 0D impurity was only detected upon performing a slow XRD scan (see Experimental Section). We could eliminate the 0D impurity by using a CsBr:PbBr$_2$ ratio of 1:1.2 in DMF. This is relevant for perovskite-based light-emitting devices as we observed that even this extremely small amount of 0D impurity in the 3D sample could significantly enhance the PL peak (Figure S2). The differences in the compositions obtained from DMSO (mainly Cs$_4$PbBr$_6$) and DMF (mainly CsPbBr$_3$) under identical precipitation conditions can be rationalized on the basis of the DLS data of the precursor solutions (Figure 1c). The formation of clusters of the lead bromide species in the DMF solution possibly templates the growth of the 3D orthorhombic phase upon the addition of the antisolvent. On the other hand, the ~1 nm-sized particles in DMSO, which are in agreement with a previous report,[34] suggest that most of the complexes in solution are isolated octahedra, making the crystallization of the 3D phase less favorable. Coordination strength of the solvent is likely a main factor responsible for these differences. DMSO is known to have a stronger coordination with Pb^{2+} compared to DMF;[30] hence, the Cs-rich phase Cs$_4$PbBr$_6$ can be easily precipitated from DMSO solution while the composition of precipitates from DMF solution is closer to the stoichiometry of the feed solution (1:1 CsBr:PbBr$_2$). Nonetheless, 3D CsPbBr$_3$ could be precipitated out from a DMSO solution by changing the antisolvent or the absolute concentration of the precursors, as discussed next.

We studied the effect of two different antisolvents on an equimolar (0.05 M) mixture of CsBr and PbBr$_2$ dissolved in DMSO. THF and dichloromethane (DCM) were chosen as antisolvents. XRD patterns of the powders are presented in Figure 2b. Simply by changing the antisolvent from THF (1:6 THF) to DCM (1:6 DCM), despite the absence of any largesized clusters, 3D perovskite is the main precipitate (see sketches in Figure 2c). Hence, it is not only the solvodynamic size of the different lead polybromide in the precursor solution that controls the phase of the obtained precipitate but also the solvent-antisolvent pair. In a 1:1 CsBr:PbBr$_2$ DMSO solution, addition of THF favors the precipitation of the Cs-rich phase (Cs$_4$PbBr$_6$) possibly due to the higher solubility of PbBr$_2$, compared to CsBr,

in this solvent-antisolvent pair. On the other hand, using DCM as an antisolvent resulted in the precipitation of the 3D phase as both precursors are relatively insoluble in the DMSO-DCM pair. Nevertheless, when an excess amount of THF is added (1:30 THF), the 3D phase is the primary formed phase (see Figure 2b). It could be possible that excess THF forces full precipitation of the $PbBr_2$ present in the precursor solution; hence, the stoichiometric 3D phase is formed. The effect of the solvodynamic size of the different lead polybromide species and solvent-antisolvent pair on the resulting Cs-Pb-Br phase is demonstrated in Figure 2c. We also explored a mixed DMSO/DMF solution and found that both THF and DCM lead to the precipitation of mainly the 3D phase with minor 0D impurity (Figure S3). Another parameter that we varied was the absolute concentration of the solution (0.05 to 0.5 M) using DMSO-THF as the solvent-antisolvent pair, and interestingly, we discovered that the lower concentration favors the precipitation of a majority of 0D, while the higher concentration favors a majority of 3D perovskites (Figure S4). The 3D precipitated from the 0.5 M DMSO solution is likely due to the high concentration that results in significant interaction between adjacent octahedra after the addition of the antisolvent.[35] In fact, upon direct addition of the antisolvent, we observed a white precipitate, which is most probably in the 0D phase or ultrasmall 3D clusters[36] that in a few seconds turned into orange-colored 3D perovskites.

XRD analysis of the precipitate from the lower absolute concentration (0.05 M) detected around 15% 3D $CsPbBr_3$(see Note S1); hence, we used a 4:1 $CsBr:PbBr_2$ ratio in order to precipitate 3D-free 0D Cs_4PbBr_6 (Figure 3, blue pattern). We observed that the (121) peak at 21.5° (2θ) corresponding to the 3D orthorhombic phase completely disappeared. However, at this precursor ratio, peaks, especially the (110) peak at 29.5° (2θ), corresponding to cubic CsBr are detected. Importantly, powders precipitated from 3.75:1 $CsBr:PbBr_2$contained detectable 3D impurity (Figure 3, green pattern). These results suggest that the formation of CsBr- and Figure 3. XRD patterns of powders precipitated from 3.75:1 (green pattern) and 4:1 (blue pattern) $CsBr:PbBr_2$ precursor solutions in DMSO. $CsPbBr_3$-free Cs_4PbBr_6 from DMSO and DMF solutions could be challenging. It is worth mentioning that the dried powders precipitated from all the different ratios were green-emitting under the UV lamp.

ssNMR on Cs-Pb-Br Powders

We carried out ^{207}Pb and ^{133}Cs solid-state nuclear magnetic resonance (ssNMR) analyses to explore the composition of our precipitates. ssNMR is a powerful characterization tool that can distinguish between different crystal structures of the same material,[37] and it can also identify the formation of amorphous and hydrated hybrid perovskite phases.[38-40] Since it is well known that the main drawback for NMR is the intrinsic poor sensitivity, we first checked the sensitivity of ssNMR in detecting perovskite impurities in the Cs-based perovskites. For this purpose, two samples were used, specifically, 3D $CsPbBr_3$ with very low 0D Cs_4PbBr_6 impurity (1:1 DMF) and 0D Cs_4PbBr_6 with very low 3D $CsPbBr_3$ impurity (3.75:1 DMSO) as suggested by their XRD patterns shown in Figure 2a (black pattern) and Figure 3 (green pattern), respectively. All ssNMR data are summarized inTable 1. The detection of the impurity phases was successful by ^{133}Cs ssNMR (Figure 4a) but not by ^{207}Pb ssNMR (Figure 4b) despite the first nuclide being quadrupolar (I = 7/2, natural abundance = 100%) while ^{207}Pb is not (I = 1/2, natural abundance = 22.6%), suggesting

higher sensitivity of ^{133}Cs ssNMR compared to its ^{207}Pb counterpart in these highly crystalline materials. It is worth noticing that the Pb signals show a fine structure with well-defined components of the multiplet originating from coupling between ^{207}Pb and the six $^{79/81}$Br atoms (I = 3/2, natural abundances of ^{79}Br = 50.54% and ^{81}Br = 49.46%), surrounding the metal ions in an octahedral geometry, as already reported for similar Cl complexes.[41] We found that ^{133}Cs ssNMR was also able to distinguish between two kinds of Cs atoms, lying in different environments in the 0D crystal structure [42] with a ratio between 2:1 and 3:1, as expected from the 0D unit cell. Moving to the "3D-free" 0D sample (4:1 DMSO), the XRD pattern of which we report in Figure 3 (blue pattern), ^{133}Cs ssNMR identified CsBr (δ_{iso} = 268 ppm), which was also detected by XRD. Importantly, ^{133}Cs ssNMR did not detect any 3D impurity in agreement with powder XRD.

Optical and Compositional Analysis of Green-Emitting Cs$_4$PbBr$_6$ Powder

We focused on the "3D-free" 0D powder (4:1 DMSO). Although XRD (Figure 3, blue pattern) and ssNMR (Figure 4, blue trace) did not detect any 3D impurity in this sample, diffuse reflectance measurements, as plotted in Figure 5a, showed absorption throughout the green region with a matching PLE (Figure S5) and a single PL emission peak at 520 nm (Figure 5a). It is worth mentioning that, in the case of our 0D powders with (3.75:1 DMSO) or without (4:1 DMSO) detectable 3D impurity, the as-precipitated wet powders are nonemissive under the UV lamp. However, they turn green-emitting after some time, whether the precipitate is left in solution, dried in a vacuum oven at 40 °C, or under N$_2$ at room temperature.

An inspection of the 4:1 DMSO sample with an optical microscope under white light (Figure S6a) and UV light (Figure S6b) revealed that the green emission is localized in bright spots scattered across the sample. This observation was further confirmed by a confocal PL microscope using 488 nm excitation (Figure 5b). The PL spectrum collected from a local area containing several emission centers peaked at ~520 nm (Figure S7), in agreement with the PL spectrum in Figure 5a. A spatial distribution of the emitting centers in three dimensions was obtained through the series of z slices of the ~40 × 40 × 5 micron volume of the sample (Figure S8). It further confirms that the emission originates from the localized spots in the sample, which are unevenly distributed across the sample. The size of the emissive domains is submicron, and resolving their shape is beyond the spatial resolution of the microscope used.

Elemental analysis of the powder was done using X-ray photoelectron spectroscopy (XPS) and energy-dispersive X-ray spectroscopy (EDS), and the compositional data is listed in Table S1. Both XPS and EDS analyses reveal that the sample is Br-deficient. This Br deficiency contradicts most reports on green-emitting 0D materials where samples were reported to be Br-rich with Pb:Br ratios up to 1:7.4.[43] The bromine deficiency in our 0D sample could be due to incorporation of other phases with lower bromine content. Next, we measured the separation between the onset of valence band maxima (VBM) and Fermi level shown in Figure 6a. We observed only a small shift when compared to reported VBM onsets of 3D CsPbBr$_3$, suggesting a possible 3D or 3D-like impurity in our 0D sample.[44] Similarly, high-resolution transmission electron microscopy (HRTEM) analysis on the 0D sample

detected a domain with lattice spacing of 5.8 Å that is indicative of 3Dlike nature (Figure 6b,c). Based on elemental analysis of different particles in the 4:1 DMSO sample, Cs_4PbBr_6 and the impurity CsBr particles were observed as individual entities and not as a composite (Figure S9).

Origin of the Green Emission

While bromine vacancy (V_{Br}) transition level energy in the Cs_4PbBr_6 was calculated by Yin et al.[13] to be 2.3 eV above the VBM, matching the green emission and, recently, V_{Br} was instead suggested to form a shallow defect level.[45] In addition, as we have previously reported,[12] the intense and sharp emission and the absence of a Stokes shift does not match with deep-trap emission.

Therefore, impurity emission would be more reasonable as the origin of the green emission. Impurity emission is in line with our confocal PL microscopy, VBM analysis, and HRTEM findings. 3D $CsPbBr_3$ could be the impurity source of the green PL emission as nonquantum-confined nanocrystals (> 8 nm) do indeed emit at around 2.39-2.41 eV.[46] However, in agreement with Wang et al.,[47] it is expected that the 3D $CsPbBr_3$ impurity might not be the only origin of the green emission. For instance, a previous report detected quantum-confined ~3 nm $CsPbBr_3$ nanocrystals embedded within larger-sized Cs_4PbBr_6 using HRTEM; however, the sample was green-emitting at 520 nm,[22] defying reported PL values for such small $CsPbBr_3$ nanocrystals.[46] In fact, PLQYs of our 0D samples with detectable 3D impurity (3.75:1 DMSO) and 3D-free (4:1 DMSO) were 25 and 50%, respectively.

Other than the known perovskite or perovskite-related phases of 3D ($CsPbBr_3$), 2D ($CsPb_2Br_5$), and 0D (Cs_4PbBr_6), Song et al.[48] reported the synthesis of a Cs_2PbBr_4 material, which they described as a 2D sheet of corner-sharing $[PbBr_6]^{4-}$ octahedra passivated by Cs^+ ions, exhibiting an absorbance and emission in the green region of the visible spectrum. This phase has not been previously reported in the phase diagram of this ternary Cs-Pb-Br system, and the synthesis of a bulk sample of Cs_2PbBr_4 appears to be challenging as the phase was suggested to be thermodynamically unstable.[49] However, this 2D sheet of corner-shared $[PbBr_6]^{4-}$ octahedra is in essence a monolayer of 3D $CsPbBr_3$. Furthermore, the 2D Ruddlesden-Popper (RP) phase of $Cs_{n+1}Pb_nBr_{3n+1}$ with $n = 1$ or 2 has also been detected as an impurity within 3D $CsPbBr_3$ nanosheets.[50] Theoretically, at $n = 1$, the Cs_2PbBr_4 layer is predicted to be a direct band-gap material, and upon introducing spin-orbit coupling (SOC) combined with a hybrid function (HSE), Yang et al.[51]calculated its band gap to be 2.29 eV.

In pure 2D perovskites such as 2D MA_2PbI_4, the difference between the band gaps of a monolayer and bulk material is theoretically calculated to be only 0.01 eV.[52] Experimentally, unlike the quasi-2D, for example, $(BA)_2(MA)_{n-1}Pb_nI_{3n+1}$(BA = butylammonium) that possesses a considerable blueshift in the PL peak position as the number of layers (n) decreases,[53]pure 2D perovskites showed insignificant differences.[54,55]Hence, a 2D perovskite structure with a small Cs cation as an interlayer spacer could explain the narrow range of PL (515 to 524 nm)[12,56] reported for the emissive 0D single crystals, powders, and nanocrystals. The proposed Cs_2PbBr_4 is different from 3-5 layered $CsPbBr_3$ nanosheets or

nanoplatelets that usually emit between 440 and 460 nm.[57,58] This discrepancy in the PL peak position could be attributed to the fact that, in the case of nanosheets and nanoplatelets, their top and bottom surfaces are covered with large organic cations such as oleylammonium or octylammonium, and hence, they could be considered as quasi-2D perovskites, leading to the pronounced blueshift in their emissions.

This hypothesis of 2D Cs_2PbBr_4 inclusions being responsible for the absorbance and emission in the green region of the visible spectrum is in agreement with work by Liu et al. [59] where they suggested the formation of $[PbBr_4]^{2-}$ intermediates (in the form of sheet structures observed in TEM) during the transformation of $CsPbBr_3$ nanocrystals to Cs_4PbBr_6 nano-crystals. It is possible that the 0D matrix stabilizes this 2D $Cs_{n+1}Pb_nBr_{3n+1}$ with the $n = 1$ (Cs_2PbBr_4) phase similar to what was detected in 3D nanosheets.[50]

Conclusions

To summarize, a mixture of $CsBr-PbBr_2$ salts dissolved in DMSO and DMF results in the formation of different lead bromide species with a solvent-dependent solvodynamic radius of the species. Solutions in DMSO feature smaller species (~1 nm of solvodynamic size) compared to the solutions in DMF, which is likely due to the stronger coordination of DMSO to Pb^{2+} compared to DMF. The size of lead bromide species influences the composition of the Cs-Pb-Br precipitates upon addition of the antisolvent: smaller species favor the formation of the Cs_4PbBr_6 phase, while larger species template the precipitation of $CsPbBr_3$. Overall, 0D Cs_4PbBr_6 has a higher tendency to be precipitated out from solutions with stronger coordinating solvents to Pb^{2+}, lower absolute concentration of the precursors, and higher $CsBr:PbBr_2$ ratios, compared to its 3D $CsPbBr_3$ counterpart. We have discussed a possible origin of the green emission in the wide-band-gap Cs_4PbBr_6 and concluded that 3D impurities might not be the only source of the emission and high PLQY. Alternatively, an impurity of 2D Cs_2PbBr_4 has been proposed, but no conclusive experimental evidence of its existence was obtained. Our work highlights the importance of the less-investigated small cation spacers (e.g., Cs or MA) in 2D perovskites. Future work would target understanding the formation mechanism of Cs_2PbBr_4 as an impurity within Cs_4PbBr_6.

Supplementary Material

Refer to Web version on PubMed Central for supplementary material.

Acknowledgments

References

(1). Saidaminov MI, Mohammed OF, Bakr OM. Low-Dimensional-Networked Metal Halide Perovskites: The Next Big Thing. ACS Energy Lett. 2017; 2:889–896.

(2). Lin H, Zhou C, Tian Y, Siegrist T, Ma B. Low-Dimensional Organometal Halide Perovskites. ACS Energy Lett. 2017:54–62.

(3). Shi E, Gao Y, Finkenauer BP, Akriti, Coffey AH, Dou L. Two-Dimensional Halide Perovskite Nanomaterials and Heterostructures. Chem Soc Rev. 2018; 47:6046–6072. [PubMed: 29564440]

(4). Gao P, Bin Mohd Yusoff AR, Nazeeruddin MK. Dimensionality Engineering of Hybrid Halide Perovskite Light Absorbers. Nat Commun. 2018; 9:5028. [PubMed: 30487520]

(5). Yuan Z, Zhou C, Tian Y, Shu Y, Messier J, Wang JC, van de Burgt LJ, Kountouriotis K, Xin Y, Holt E, Schanze K, et al. One-Dimensional Organic Lead Halide Perovskites with Efficient Bluish White-Light Emission. Nat Commun. 2017; 8

(6). Liu M, Zhao J, Luo Z, Sun Z, Pan N, Ding H, Wang X. Unveiling Solvent-Related Effect on Phase Transformations in $CsBr-PbBr_2$ System: Coordination and Ratio of Precursors. Chem Mater. 2018; 30:5846–5852.

(7). Zhao Y, Zhu K. Organic-Inorganic Hybrid Lead Halide Perovskites for Optoelectronic and Electronic Applications. Chem Soc Rev. 2016; 45:655–689. [PubMed: 26645733]

(8). Adinolfi V, Yuan M, Comin R, Thibau ES, Shi D, Saidaminov MI, Kanjanaboos P, Kopilovic D, Hoogland S, Lu ZH, Bakr OM, Sargent EH. The in-Gap Electronic State Spectrum of Methylammonium Lead Iodide Single-Crystal Perovskites. Adv Mater. 2016; 28:3406–3410. [PubMed: 26932458]

(9). Cha J-H, Han JH, Yin W, Park C, Park Y, Ahn TK, Cho JH, Jung D-Y. Photoresponse of $CsPbBr_3$ and Cs_4PbBr_6 Perovskite Single Crystals. J Phys Chem Lett. 2017; 8:565–570. [PubMed: 28067051]

(10). Yin J, Zhang Y, Bruno A, Soci C, Bakr OM, Brédas JL, Mohammed OF. Intrinsic Lead Ion Emissions in ZeroDimensional Cs_4PbBr_6 Nanocrystals. ACS Energy Lett. 2017; 2:2805–2811.

(11). Zhang Y, Saidaminov MI, Dursun I, Yang H, Murali B, Alarousu E, Yengel E, Alshankiti BA, Bakr OM, Mohammed OF. Zero-Dimensional Cs_4PbBr_6 Perovskite Nanocrystals. J Phys Chem Lett. 2017; 8:961–965. [PubMed: 28181438]

(12). Akkerman QA, Abdelhady AL, Manna L. ZeroDimensional Cesium Lead Halides: History, Properties, and Challenges. J Phys Chem Lett. 2018; 9:2326–2337. [PubMed: 29652149]

(13). Yin J, Yang H, Song K, El-Zohry AM, Han Y, Bakr OM, Brédas JL, Mohammed OF. Point Defects and Green Emission in Zero-Dimensional Perovskites. J Phys Chem Lett. 2018; 9:5490–5495. [PubMed: 30180582]

(14). >Seth S, Samanta A. Fluorescent Phase-Pure Zero-Dimensional Perovskite-Related Cs_4PbBr_6 Microdisks: Synthesis and Single-Particle Imaging Study. J Phys Chem Lett. 2017; 8:4461–4467. [PubMed: 28862458]

(15). De Bastiani M, Dursun I, Zhang Y, Alshankiti BA, Miao X-H, Yin J, Yengel E, Alarousu E, Turedi B, Almutlaq JM, Saidaminov MI, et al. Inside Perovskites: Quantum Luminescence from Bulk Cs_4PbBr_6 Single Crystals. Chem Mater. 2017; 29:7108–7113.

(16). Wells HL. Über Die Cäsium-Und Kalium-Bleihalogenide. Z Anorg Chem. 1893; 3:195–210.

(17). Nikl M, Mihokova E, Nitsch K, Somma F, Giampaolo C, Pazzi GP, Fabeni P, Zazubovich S. Photoluminescence of Cs_4PbBr_6 Crystals and Thin Films. Chem Phys Lett. 1999; 306:280–284.

(18). Kondo S, Amaya K, Saito T. Localized Optical Absorption in Cs_4PbBr_6. J Phys Condens Matter. 2002; 14:2093–2099.

(19). Akkerman QA, Park S, Radicchi E, Nunzi F, Mosconi E, De Angelis F, Brescia R, Rastogi P, Prato M, Manna L. Nearly Monodisperse Insulator Cs_4PbX_6 (X = Cl, Br, I) Nanocrystals, Their Mixed Halide Compositions, and Their Transformation into $CsPbX_3$ Nanocrystals. Nano Lett. 2017; 17:1924–1930. [PubMed: 28196323]

(20). Quan LN, Quintero-Bermudez R, Voznyy O, Walters G, Jain A, Fan JZ, Zheng X, Yang Z, Sargent EH. Highly Emissive Green Perovskite Nanocrystals in a Solid State Crystalline Matrix. Adv Mater. 2017; 29

(21). Xu J, Huang W, Li P, Onken DR, Dun C, Guo Y, Ucer KB, Lu C, Wang H, Geyer SM, Williams RT, Carroll DL. Imbedded Nanocrystals of CsPbBr$_3$ in Cs$_4$PbBr$_6$: Kinetics, Enhanced Oscillator Strength, and Application in Light-Emitting Diodes. Adv Mater. 2017; 29

(22). Chen X, Zhang F, Ge Y, Shi L, Huang S, Tang J, Lv Z, Zhang L, Zou B, Zhong H. Centimeter-Sized Cs$_4$PbBr$_6$ Crystals with Embedded CsPbBr$_3$ Nanocrystals Showing Superior Photoluminescence: Nonstoichiometry Induced Transformation and LightEmitting Applications. Adv Funct Mater. 2018

(23). Xuan T, Lou S, Huang J, Cao L, Yang X, Li H, Wang J. Monodisperse and Brightly Luminescent CsPbBr$_3$/Cs$_4$PbBr$_6$ Perovskite Composite Nanocrystals. Nanoscale. 2018; 10:9840–9844. [PubMed: 29785438]

(24). Riesen N, Lockrey M, Badek K, Riesen H. On the Origins of the Green Luminescence in the "Zero-Dimensional Perovskite" Cs$_4$PbBr$_6$: Conclusive Results from Cathodoluminescence Imaging. Nanoscale. 2019; 11:3925–3932. [PubMed: 30761398]

(25). Ling Y, Tan L, Wang X, Zhou Y, Xin Y, Ma B, Hanson K, Gao H. Composite Perovskites of Cesium Lead Bromide for Optimized Photoluminescence. J Phys Chem Lett. 2017; 8:3266–3271. [PubMed: 28677389]

(26). Baranov D, Toso S, Imran M, Manna L. Investigation into the Photoluminescence Red Shift in Cesium Lead Bromide Nanocrystal Superlattices. J Phys Chem Lett. 2019; 10:655–660. [PubMed: 30676762]

(27). Yoon SJ, Stamplecoskie KG, Kamat PV. How Lead Halide Complex Chemistry Dictates the Composition of Mixed Halide Perovskites. J Phys Chem Lett. 2016; 7:1368–1373. [PubMed: 27007695]

(28). Oldenburg K, Vogler A. Electronic Spectra and Photochemistry of Tin(II), Lead(II), Antimony(III), and Bismuth(III) Bromide Complexes in Solution. Z Naturforsch B. 1993; 48:1519–1523.

(29). Rahimnejad S, Kovalenko A, Forés SM, Aranda C, Guerrero A. Coordination Chemistry Dictates the Structural Defects in Lead Halide Perovskites. ChemPhysChem. 2016; 17:2795–2798. [PubMed: 27338309]

(30). Hamill JC Jr, Schwartz J, Loo YL. Influence of Solvent Coordination on Hybrid Organic–Inorganic Perovskite Formation. ACS Energy Lett. 2018; 3:92–97.

(31). Wu Y, Islam A, Yang X, Qin C, Liu J, Zhang K, Peng W, Han L. Retarding the Crystallization of PbI$_2$ for Highly Reproducible Planar-Structured Perovskite Solar Cells Via Sequential Deposition. Energy Environ Sci. 2014; 7:2934–2938.

(32). Yan K, Long M, Zhang T, Wei Z, Chen H, Yang S, Xu J. Hybrid Halide Perovskite Solar Cell Precursors: Colloidal Chemistry and Coordination Engineering Behind Device Processing for High Efficiency. J Am Chem Soc. 2015; 137:4460–4468. [PubMed: 25780941]

(33). McMeekin DP, Wang Z, Rehman W, Pulvirenti F, Patel JB, Noel NK, Johnston MB, Marder SR, Herz LM, Snaith HJ. Crystallization Kinetics and Morphology Control of Formamidinium-Cesium Mixed-Cation Lead Mixed-Halide Perovskite Via Tunability of the Colloidal Precursor Solution. Adv Mater. 2017; 29

(34). Wei Z, Perumal A, Su R, Sushant S, Xing J, Zhang Q, Tan ST, Demir HV, Xiong Q. Solution-Processed Highly Bright and Durable Cesium Lead Halide Perovskite Light-Emitting Diodes. Nanoscale. 2016; 8:18021–18026. [PubMed: 27722383]

(35). Stevenson J, Sorenson B, Subramaniam VH, Raiford J, Khlyabich PP, Loo Y-L, Clancy P. Mayer Bond Order as a Metric of Complexation Effectiveness in Lead Halide Perovskite Solutions. Chem Mater. 2017; 29:2435–2444.

(36). Xu Y, Zhang Q, Lv L, Han W, Wu G, Yang D, Dong A. Synthesis of Ultrasmall CsPbBr$_3$ Nanoclusters and Their Transformation to Highly Deep-Blue-Emitting Nanoribbons at Room Temperature. Nanoscale. 2017:17248. [PubMed: 29114683]

(37). Bureau B, Silly G, Buzaré JY. CP-MAS [207]Pb with ^{19}F Decoupling NMR Spectroscopy: Medium Range Investigation in Fluoride Materials. Solid State Nucl Magn Reson. 1999; 15:79–89. [PubMed: 10670899]

(38). Rosales BA, Men L, Cady SD, Hanrahan MP, Rossini AJ, Vela J. Persistent Dopants and phase Segregation in Organolead Mixed-Halide perovskites. Chem Mater. 2016; 28:6848–6859.

(39). Askar AM, Bernard GM, Wiltshire B, Shankar K, Michaelis VK. Multinuclear Magnetic Resonance Tracking of Hydro, Thermal and Hydrothermal Decomposition of $CH_3NH_3pbI_3$. J Phys Chem C. 2017; 121:1013–1024.

(40). Rosales BA, Hanrahan MP, Boote BW, Rossini AJ, Smith EA, Vela J. Lead Halide perovskites: Challenges and Opportunities in Advanced Synthesis and Spectroscopy. ACS Energy Lett. 2017; 2:906–914.

(41). Wrackmeyer, B, Horchler, K. ^{207}pb-NMR parametersAnnual Reports on NMR Spectroscopy. Webb, GA, editor. Vol. 22. Academic Press; 1990. 249–306.

(42). Hu M, Ge C, Yu J, Feng J. Mechanical and Optical properties of Cs_4BX_6 (B = pb, Sn; X = Cl, Br, I) Zero-Dimension perovskites. J Phys Chem C. 2017; 121:27053–27058.

(43). Yang H, Zhang Y, pan J, Yin J, Bakr OM, Mohammed OF. Room-Temperature Engineering of All-Inorganic perovskite Nanocrsytals with Different Dimensionalities. Chem Mater. 2017; 29:8978–8982.

(44). Endres J, Egger DA, Kulbak M, Kerner RA, Zhao L, Silver SH, Hodes G, Rand BP, Cahen D, Kronik L, Kahn A. Valence and Conduction Band Densities of States of Metal Halide perovskites: A Combined Experimental–Theoretical Study. J Phys Chem Lett. 2016; 7:2722–2729. [PubMed: 27364125]

(45). Jung Y-K, Calbo J, park J-S, Wahlley LD, Kim S, Walsh A. Lumínescence of polybromide Defects in Cs_4pbBr_6 . ChemRxiv. 2019; doi: 10.26434/chemrxiv.7629467

(46). Almeida G, Goldoni L, Akkerman Q, Dang Z, Khan AH, Marras S, Moreels I, Manna L. Role of Acid-Base Equilibria in the Size, Shape, and phase Control of Cesium Lead Bromide Nanocrystals. ACS Nano. 2018; 12:1704–1711. [PubMed: 29381326]

(47). Wang K-H, Yang J-N, Ni Q-K, Yao H-B, Yu S-H. Metal Halide perovskite Supercrystals: Gold-Bromide Complex Triggered Assembly of $CspbBr_3$ Nanocubes. Langmuir. 2018; 34:595–602. [PubMed: 29251940]

(48). Song J, Xu L, Li J, Xue J, Dong Y, Li X, Zeng H. Monolayer and Few-Layer All-Inorganic perovskites as a New Family of Two-Dimensional Semiconductors for printable Optoelectronic Devices. Adv Mater. 2016; 28:4861–4869. [PubMed: 27110705]

(49). Li J, Yu Q, He Y, Stoumpos CC, Niu G, Trimarchi GG, Guo H, Dong G, Wang D, Wang L, Kanatzidis MG. $Cs_2pbI_2Cl_2$, All-Inorganic Two-Dimensional Ruddlesden-popper Mixed Halide perovskite with Optoelectronic Response. J Am Chem Soc. 2018; 140:11085–11090. [PubMed: 30081628]

(50). Yu Y, Zhang D, Yang p. Ruddlesden–popper phase in TwoDimensional Inorganic Halide perovskites: A plausible Model and the Supporting Observations. Nano Lett. 2017; 17:5489–5494. [PubMed: 28796526]

(51). Yang J-H, Yuan Q, Yakobson BI. Chemical Trends of Electronic properties of Two-Dimensional Halide perovskites and Their potential Applications for Electronics and Optoelectronics. J Phys Chem C. 2016; 120:24682–24687.

(52). Zhu X, Xu Z, Zuo S, Feng J, Wang Z, Zhang X, Zhao K, Zhang J, Liu H, priya S, Liu SF, Yang D. Vapor-Fumigation for Record Efficiency Two-Dimensional perovskite Solar Cells with Superior Stability. Energy Environ Sci. 2018; 11:3349–3357.

(53). Stoumpos CC, Cao DH, Clark DJ, Young J, Rondinelli JM, Jang JI, Hupp JT, Kanatzidis MG. Ruddlesden-popper Hybrid Lead Iodide perovskite 2D Homologous Semiconductors. Chem Mater. 2016; 28:2852–2867.

(54). Dou L, Wong AB, Yu Y, Lai M, Kornienko N, Eaton SW, Fu A, Bischak CG, Ma J, Ding T, Ginsberg NS, et al. Atomically Thin Two-Dimensional Organic-Inorganic Hybrid perovskites. Science. 2015; 349:1518–1521. [PubMed: 26404831]

(55). Yin H, Jin L, Qian Y, Li X, Wu Y, Bowen MS, Kaan D, He C, Wozniak DI, Xu B, Lewis AJ, Shen W, Chen K, Dobereiner GE, Zhao Y, Wayland BB, Rao Y. Excitonic and Confinement Effects of 2D Layered $(C_{10}H_{21}NH_3)_2pbBr_4$ Single Crystals. ACS Appl Energy Mater. 2018; 1:1476–1482.

(56). Almutlaq J, Yin J, Mohammed OF, Bakr OM. The Benefit and Challenges of Zero-Dimensional perovskites. J Phys Chem Lett. 2018; 9:4131–4138. [PubMed: 29953235]

(57). Akkerman QA, Motti SG, Srimath Kandada AR, Mosconi E, D'Innocenzo V, Bertoni G, Marras S, Kamino BA, Miranda L, De Angelis F, petrozza A, prato M, Manna L. Solution Synthesis Approach to Colloidal Cesium Lead Halide perovskite Nanoplatelets with Monolayer-Level Thickness Control. J Am Chem Soc. 2016; 138:1010–1016. [PubMed: 26726764]

(58). Shamsi J, Dang Z, Bianchini p, Canale C, Di Stasio F, Brescia R, prato M, Manna L. Colloidal Synthesis of Quantum Confined Single Crystal CspbBr$_3$ Nanosheets with Lateral Size Control up to the Micrometer Range. J Am Chem Soc. 2016; 138:7240–7243. [PubMed: 27228475]

(59). Liu Z, Bekenstein Y, Ye X, Nguyen SC, Swabeck J, Zhang D, Lee S-T, Yang P, Ma W, Alivisatos AP. Ligand Mediated Transformation of Cesium Lead Bromide perovskite Nanocrystals to Lead Depleted Cs$_4$pbBr$_6$ Nanocrystals. J Am Chem Soc. 2017; 139:5309–5312. [PubMed: 28358191]
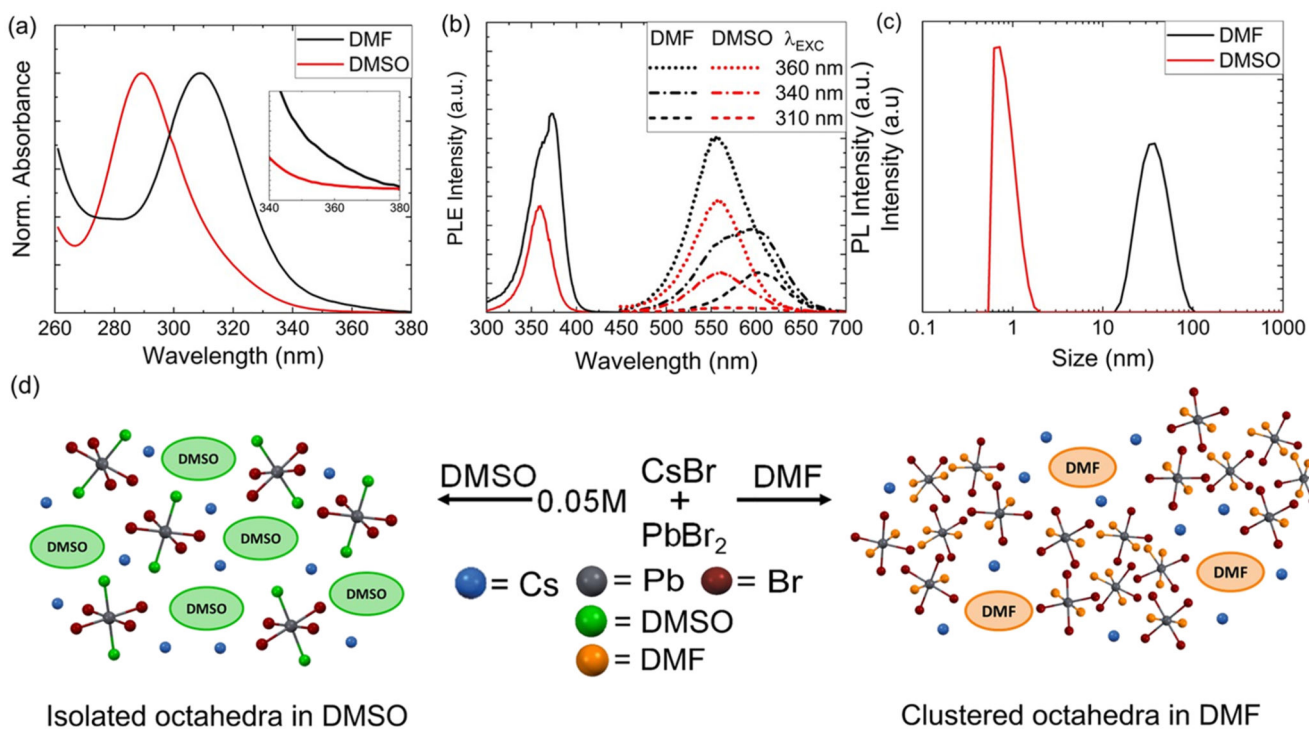
Figure 1.
(a) Normalized absorbance and (b) PLE (solid lines) and PL (dotted and dashed lines)
spectra of 0.05 M 1:1 $CsBr:PbBr_2$ precursor solutions in DMF and DMSO. PLE is reported
at the highest intensity emission (560 nm), while PL is recorded at different excitation
wavelengths. (c) Corresponding DLS measurements. (d) Scheme illustrating the photoactive
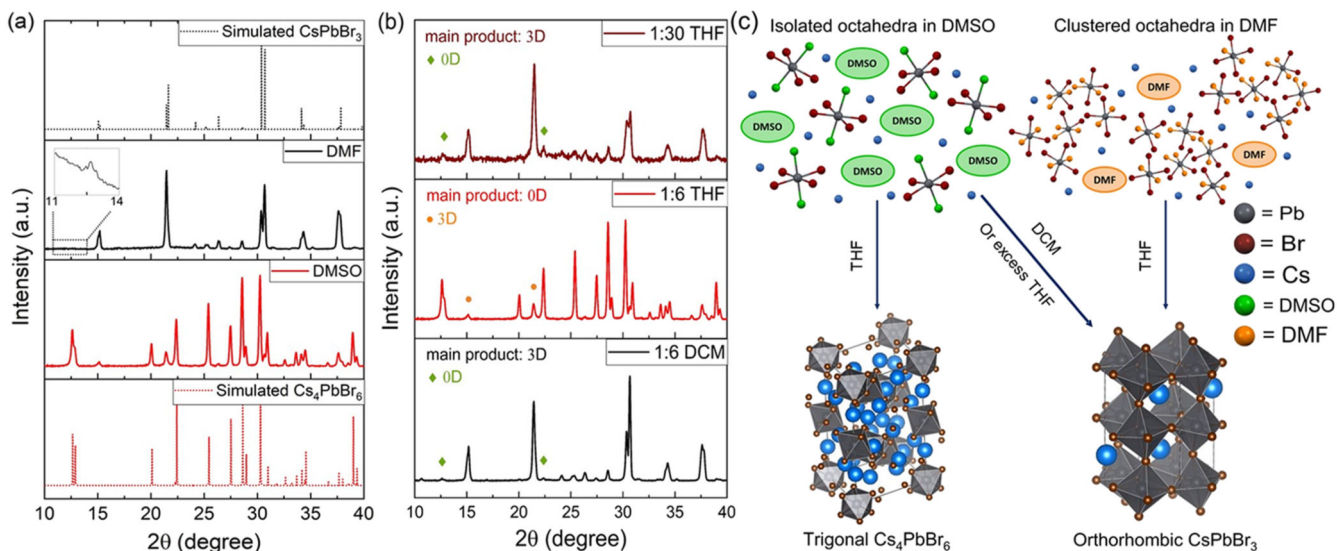species formed upon dissolving 0.05 M 1:1 $CsBr:PbBr_2$ in DMSO and DMF.

Figure 2.
(a) XRD patterns of Cs-Pb-Br powders precipitated from 0.05 M 1:1 $CsBr:PbBr_2$ DMSO and DMF solutions along with simulated patterns for trigonal Cs_4PbBr_6 (ICSD-162158) and orthorhombic $CsPbBr_3$ (ICSD-97851) phases. (b) XRD of Cs-Pb-Br powders precipitated from different DMSO:antisolvent volume ratios. (c) Scheme illustrating the effect of the solvodynamic size and solvent–antisolvent pair on the formed phases.
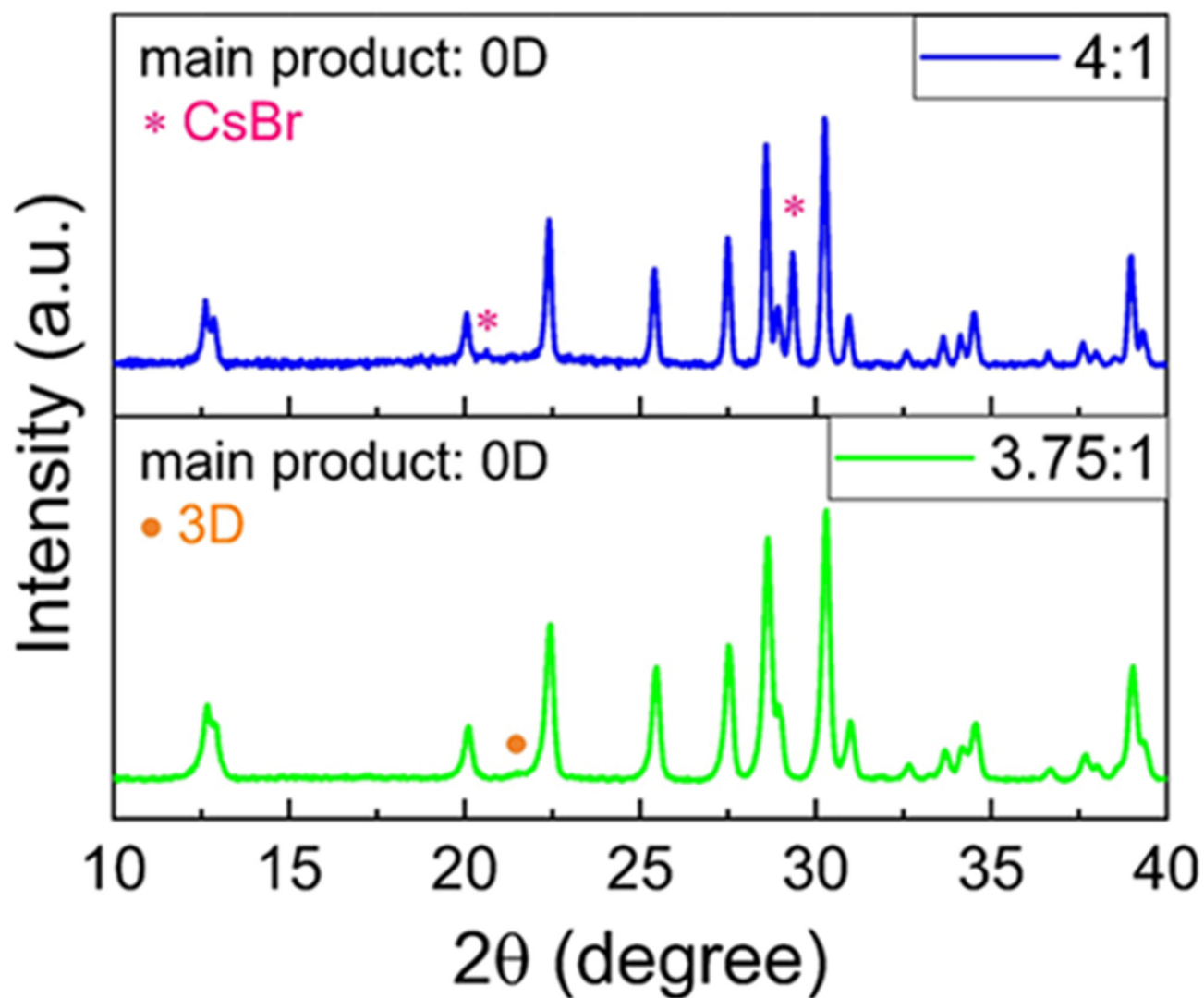
Figure 3.
XRD patterns of powders precipitated from 3.75:1 (green pattern) and 4:1 (blue pattern)
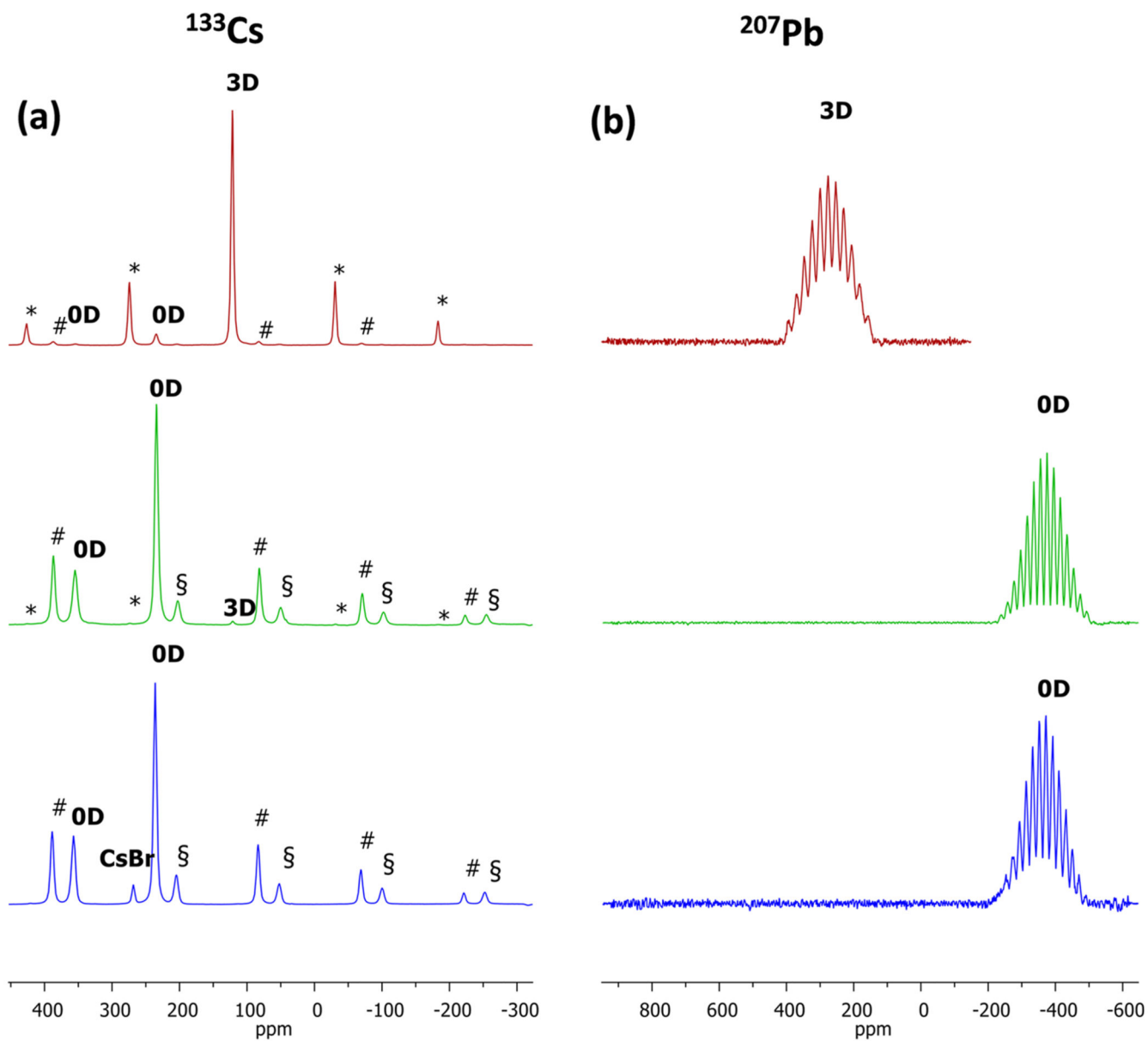CsBr:PbBr$_2$ precursor solutions in DMSO.

Figure 4.
(a) ^{133}Cs and (b) ^{207}Pb ssNMR spectra (10 kHz MAS, 11.75 T, 312 K) of the samples 1:1 DMF (red trace), 3.75:1 DMSO (green trace), and 4:1 DMSO (blue trace). The asterisks (*) mark the spinning sidebands (SSBs) of the 3D phase signal, the section signs (§) mark the SSB of the less intense 0D peak, and the pound signs (#) mark the SSB of the more intense 0D peak.
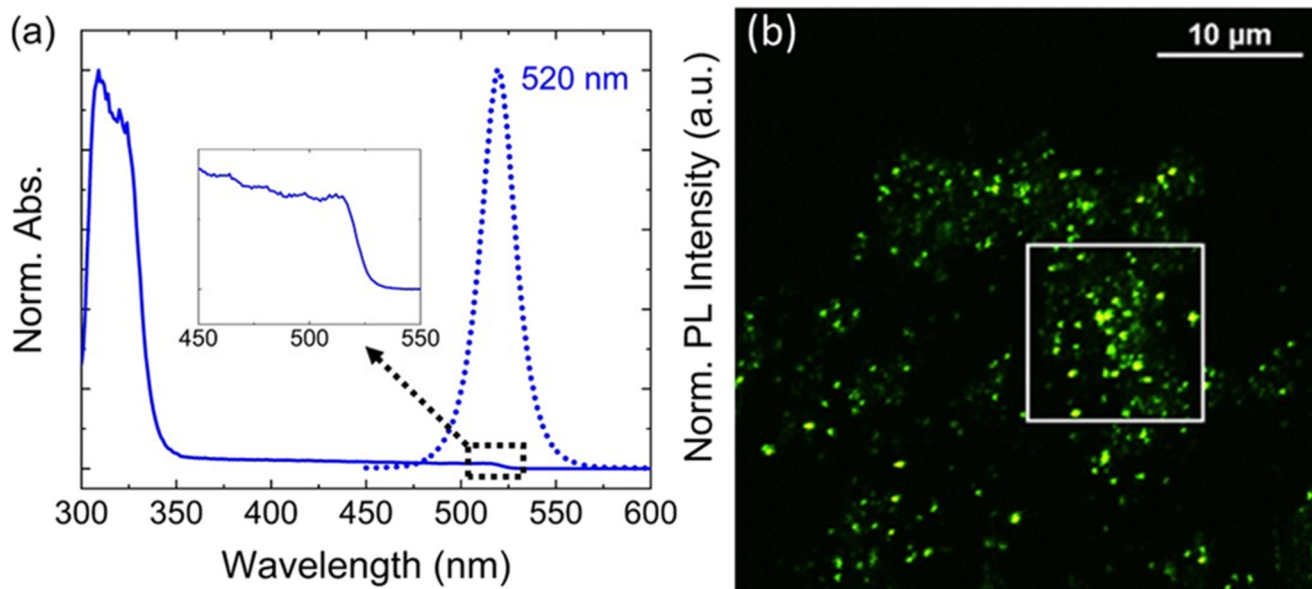
Figure 5.
(a) Optical absorption (solid line) of the 4:1 DMSO powder sample obtained by converting reflectance (R) to absorption using the Kubelka-Munk equation,[6] $F(R)=(1-R)^2/2R$, and PL emission (dotted line) at the excitation wavelength of 405 nm. (b) Confocal PL microscopy image recorded with 488 nm excitation; the PL spectrum from an area highlighted by the white square is shown in Figure S7
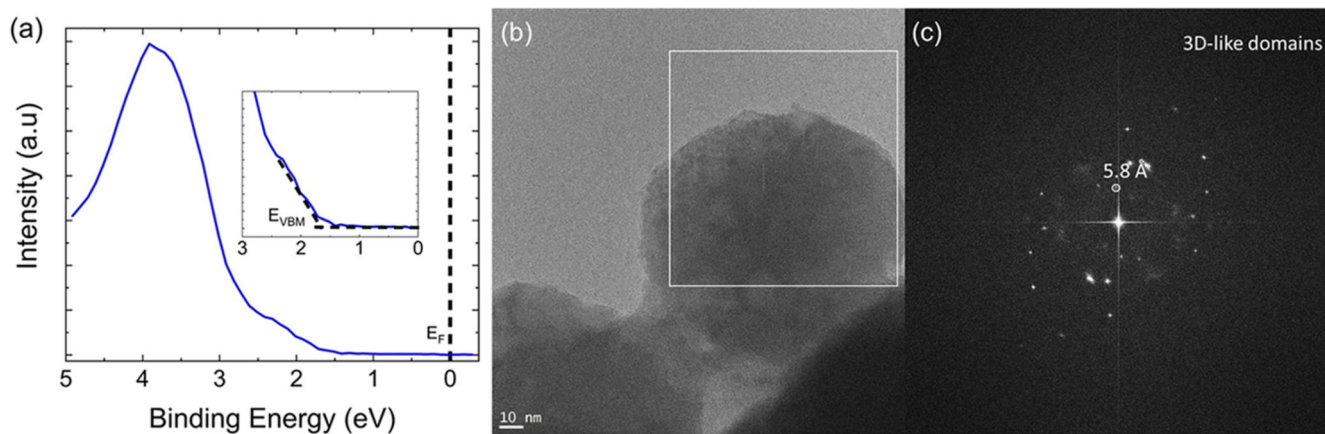
Figure 6.
(a) XPS results on the 4:1 DMSO sample showing the separation between the onset of valence band maxima (VBM) and Fermi level. (b) HRTEM image and (c) corresponding fast Fourier transform (FFT) of the white square area showing lattice spacing of 5.8 Å.

Table 1

Summary of Powder XRD and [133]Cs and [207]Pb ssNMR Analysis on Three Different Samples[a]

sample CsBr:PbBr2 solvent	powder XRD	133Cs ssNMR	207Pb ssNMR
1:1 DMF	3D + 0D impurity	3D (120 ppm) + 0D impurity	3D only (246 ppm, $^1 J_{\text{Pb-Br}}$ = 2425 Hz)
3.75:1 DMSO	0D + 3D impurity	0D (354 and 233.6 ppm) + 3D impurity	0D only (−373 ppm, $^1 J_{\text{Pb-Br}}$ = 2050 Hz)
4:1 DMSO	0D + CsBr	0D + CsBr (268 ppm)	0D only

[a]In brackets, the δ_{iso} (ppm) of the different phases is reported. For the [207]pb signal, the scalar coupling constant $^1 J_{\text{pb-Br}}$ typical for these systems is also included.[41]